Droplet shape relaxation in a four-channel microfluidic hydrodynamic trap

Shweta Narayan [1], Davis B. Moravec [2], Andrew J. Dallas [2], and Cari S. Dutcher [1,3,*]

[1]*Department of Mechanical Engineering, University of Minnesota–Twin Cities, Minneapolis, Minnesota 55414, USA*
[2]*Donaldson Company Inc., Bloomington, Minnesota 55431, USA*
[3]*Department of Chemical Engineering and Materials Science, University of Minnesota–Twin Cities, Minneapolis, Minnesota 55414, USA*

Two-phase liquid-liquid systems are prevalent in a range of commercial and environmental applications. Understanding the behavior of liquid-liquid systems under various processing conditions requires the study of droplet dynamics under precisely controlled flow fields. Here we trap and control the position of droplets in a microfluidic trap to study their dynamics using hydrodynamic forces alone without an external field. The hydrodynamic trap is adapted from a previously implemented "Stokes trap" by incorporating a drop-on-demand system to generate droplets at a T-junction geometry on the same microfluidic chip. Using the hydrodynamic trap, confined droplet dynamics in response to perturbation are studied by applying a millisecond-pressure pulse to deform trapped droplets. Droplet shape relaxation after cessation of the pressure pulse follows an exponential decay. The characteristic droplet shape relaxation time is obtained from the shape decay curves, for aqueous glycerol droplets of varying viscosities in the dispersed phase with light and heavy mineral oils in the continuous phase. Systems were chosen to provide similar equilibrium interfacial tensions (5–10 mN/m) with wide variations of viscosity ratios. It is found that the droplet shape relaxation in the moderately confined regime shows a strong dependence on droplet radius, and a weaker dependence on the ratio of dispersed to continuous phase viscosity. An empirical scaling relationship is developed, and relaxation times from the experiments are compared to theoretical relaxation times for the limiting regime of unconfined droplets. The droplet response in the moderately confined regime differs from both limiting regimes of unconfined and highly confined droplets with regards to the radius scaling. Droplet shape relaxation time can be used inform the response of droplets in an emulsion when subjected to transient flows in various processing conditions. Finally, an application of this platform for directly visualizing droplet coalescence in planar extensional flow is presented. The microfluidic four-channel hydrodynamic trap can thus be applied for studying the fundamental physics of droplet deformation and droplet-droplet interactions on the microscale.

I. INTRODUCTION

Emulsions, or suspensions of one fluid in another immiscible fluid, are present in various applications, including oil recovery [1,2], food processing [3–5], atmospheric aerosols [6], drug delivery [7–9], and cosmetic products [10–12]. A fundamental understanding of the physical and chemical conditions leading to emulsion stability and breakup is essential for improving processes involving

---

*Corresponding author: cdutcher@umn.edu

emulsions. Emulsions are subjected to complex processing conditions such as pumping, mixing, extrusion or spraying, under shear or extensional flow fields [13]. For example, micrometer-sized water droplets can become entrained in diesel fuel in automobile engines. Once entrained, the droplets can cause corrosion and pitting of components [14]. In order to remove these droplets, coalescing filters are used, where the drops are subjected to complex shear and extensional flows under confinement. In coalescing filters and other emulsion processing equipment, individual droplets can be distorted, interact or coalesce with other droplets. Better understanding of the response of a confined droplet to a perturbation in shape can yield insights into the emulsion dynamics in confined flows. In this work, we identify three key areas where studies of droplet response during emulsion processing are undercharacterized, namely, (1) droplet response to sudden cessation of flow (characterized by a shape relaxation time), (2) effect of dispersed phase viscosity on droplet shape relaxation in liquid-liquid systems, and (3) effect of confinement on droplet shape relaxation time.

In prior single-droplet deformation studies, experimental and theoretical approaches have been used to characterize the behavior of discrete droplets suspended in another fluid phase. From a theoretical perspective, seminal papers by Lord Rayleigh [15], Sir Horace Lamb [16] and G. I. Taylor [17,18] laid the foundation for single-droplet deformation studies, providing the analytical solutions for droplet behavior in emulsions. Of particular relevance to the current study are the solutions derived by Lamb [16], who obtained a theoretical expression for the damping time of a liquid globe in a fluid of negligible density and viscosity and for a spherical bubble oscillating about an equilibrium shape, both in the inviscid limit. Taking this to the next step, Chandrasekhar [19] extended this derivation for a droplet of finite viscosity in an inviscid outer phase (e.g., air) or a bubble in a fluid of finite viscosity to obtain expressions for the oscillation frequency and damping time, based on the fluid viscosity and surface tension. Most notably, Chandrasekhar identified a critical value of drop/outer fluid viscosity above which the droplet or bubble would not oscillate but return to its equilibrium shape in an aperiodic manner exhibiting a slow decay. Suryanarayana and Bayazitoglu [20] solved Chandrasekhar's equations numerically to illustrate aperiodic (or periodic) motion in the limit of high (or low) droplet viscosity. Furthermore, Miller and Scriven [21] derived analytical expressions for oscillation frequency and damping time of a droplet of finite viscosity suspended in another quiescent medium of a finite viscosity. Finally, these cases were defined for free interfaces, inextensible interfaces or interfaces populated by insoluble and soluble surfactants by Miller and Scriven, Lu and Apfel, and others [21–25]. These early works have provided the foundation for more advanced theoretical studies of droplet deformation in shear and extensional flows by Barthes-Biesèl and Acrivos [26], Cox [27], and others [28–31].

Experimentally, devices which trap droplets at a stagnation point can be applied towards measurement of the droplet's response to perturbation. Historically, "droplet tweezers" or "droplet traps" have been considered a highly tunable and versatile method for studying single-droplet dynamics. Most techniques for capturing or trapping particles or droplets employ an external field such as optical, electric or acoustic fields to exert a trapping force. For droplet-in-air systems, optical tweezers have been employed widely for trapping droplets and particles and measuring their properties, including viscosity and surface tension, from droplet shape oscillations [32–34]. Similarly, acoustic tweezers have been employed for trapping droplet arrays and measuring material properties from drop deformation dynamics [22–24]. For liquid-liquid systems, the four-roll mill developed originally by Taylor [18] has been miniaturized and automated by Leal and coworkers [35–37] to study drop deformation under controlled flow fields. The four-roll mill has been employed extensively to study droplet deformation under shear and extensional flows; for example, Stone *et al.* [37,38] employed this apparatus to investigate the transient response of droplets in a suspending medium (with varying viscosity ratios) upon cessation of flow. While the relaxation time was found to be controlled solely by interfacial tension, the qualitative features of the deformation exhibited a dependence on viscosity ratio. Although the dynamics of the problem here are complicated and depend on the initial elongation of the drop [39], when drops were subjected to an initially large deformation, drop breakup was observed upon cessation of flow in low viscosity ratio cases, whereas

for the highest viscosity ratio, Stone *et al.* [38] observed a slow relaxation of the droplet back to a steady spherical shape. This finding indicates that the viscosity ratio and initial elongation plays a key role in droplet relaxation dynamics when drops are subjected to flow transients.

Droplet microfluidic devices have also been used for a wide range of experimental studies on droplet dynamics including deformation, coalescence and breakup. Christopher *et al.* used a simple T-junction microfluidic geometry to study coalescence and breakup of slug-shaped droplets as a function of capillary number, finding a critical capillary number for coalescence and splitting which scales with slug curvature and viscosity ratio [40]. Similarly, flow through a microfluidic cross-slot device has been employed to study slender shapes of highly viscous droplets as a function of capillary number [41]. Deformation of droplets flowing through a microfluidic contraction or expansion has also been extensively used as a method to measure interfacial tension between two fluid phases [6,14,42–44]. The effect of solid particles at the liquid-liquid interface on droplet coalescence has been studied by colliding droplets generated at opposing T-junctions by Zhou *et al.* [43]. Coalescence and breakup of a large number of droplets in an emulsion has also been studied using geometric expansions, cross-slots or contractions in microfluidic devices [44–48]. While these microfluidic methods provide valuable information about droplet deformation and coalescence, they lack precise control over droplet position and are conducted in strong bulk flow environments, such that the velocity of fluid in the outer phase strongly influences droplet dynamics.

A microfluidic version of the four-roll mill was developed by Hudson *et al.* [49], capable of generating both extensional and shear flows. Schroeder and coworkers first developed a microfluidic hydrodynamic trap, which employed a two-layer microfluidic device (with a control layer and a fluidic layer) with feedback control for trapping particles at a stagnation point in a cross-slot using on-chip membrane valves [50–52]. The microfluidic hydrodynamic trap was improved further by Shenoy *et al.* [53] by replacing the two-layer membrane valve device with a single-layer microfluidic device, where trapping is achieved by controlling the flow rates in the channels forming the cross-slot using an optimization algorithm for control. This device, called a "Stokes trap" can be used for gentle hydrodynamic trapping and steering of particles in the microfluidic device. Moreover, the number of stagnation points in a Stokes trap can be increased by increasing the number of channels, such that two stagnation points can be employed to trap two particles simultaneously to study particle collisions [53,54]. The Stokes trap has previously been implemented for studying vesicle and polymer dynamics at a stagnation point [53–56]. Ramachandran and coworkers employed a diamond-shaped hydrodynamic cross-slot to measure dynamic interfacial tension for bitumen-water systems as well as to study soft particle assembly in flow [54,57,58]. In a more recent work, Narayan *et al.* [59] employed a Stokes trap to measure the film drainage time for droplet coalescence as a function of droplet speed, diameter, and surfactant concentration for water-in-oil emulsions. In this work, we present the first experiments, to the best of our knowledge, employing a microfluidic hydrodynamic trap to study droplet dynamics and response to flow transients under confinement.

Finally, while theory and experiments pertaining to droplet response in an unconfined flow field abound in literature, relatively fewer studies consider the effect of confinement on a droplet's shape response to perturbation. Particularly in microfluidic devices, droplets are inevitably subjected to forces due to the confining walls of the channel, resulting in a combination of shear and extensional fields acting on droplets [42]. Previous studies on the effect of degree of confinement on the deformation of drops in a microfluidic extensional flow device have revealed that increasing confinement tends to enhance droplet deformation at a given strain rate [60]. In shear flows, confinement has been shown to slow down droplet relaxation by several researchers [61–64]. In fact, Minale *et al.* found that for a non-Newtonian continuous phase, e.g., Boger fluid, a single relaxation time can be used for droplet shape relaxation dynamics when the drops are highly confined, unlike for unconfined drops, where two relaxation timescales have been identified [64]. Ulloa *et al.* [65] used a flow-through microfluidic cross-slot device to study relaxation of confined droplets in an extensional flow field. The relaxation of highly confined droplets in Hele-Shaw geometries has been studied numerically by Gallaire and coworkers [66–68] and experimentally using microfluidics by Kerdraon *et al.* [69]. Understanding the droplet shape relaxation dynamics in confined flow fields can be critical for

understanding dynamics that occur during the transient flows of emulsions in various processing applications, including filtration and mixing [70]. Moreover, while highly confined droplets in the Hele-Shaw regime have been studied in the past, droplet confinement in applications can be anywhere from fully unconfined to moderately to highly confined. Here we investigate the hitherto largely unexplored regime of moderately confined droplets.

In this work, we present experiments employing a microfluidic hydrodynamic trap that enables new measurements of the dynamic response of moderately confined droplets to flow perturbations. The Stokes trap developed by Shenoy *et al.* [53] is modified to include on-chip LabVIEW-controlled droplet formation using a droplet-on-demand technique. Droplets formed in the device are gently trapped at the center of a cross-slot with hydrodynamic forces alone using feedback control, as discussed in Sec. II. In Sec. III, results from droplet deformation and relaxation experiments are presented. Droplet shape relaxation times are measured over a range of viscosity ratios and droplet sizes. An empirical scaling for the dependence of the relaxation time on droplet size and viscosity ratio at weak to moderate confinements is presented in Sec. III A. In addition to understanding transient drop dynamics in confined geometries, this empirical scaling method could potentially be used to analyze drop retraction experiments in microfluidics for measuring interfacial tension [71]. With this experiment, we aim to address the key areas identified previously where current experimental investigations are lacking: (1) droplet relaxation time in response to perturbations, (2) effect of viscosity ratio on droplet relaxation time, and (3) effect of weak to moderate confinement on drop shape relaxation. Finally, an application of the hydrodynamic trap for studying binary droplet coalescence is highlighted in Sec. III D.

II. METHODS AND MATERIALS

A. Device fabrication and experimental setup

The microfluidic device used for hydrodynamic trapping is fabricated using standard soft-lithography methods [72–74]. Briefly, the mask design for a four-inch silicon wafer is created using DraftSight (Dassault Systèmes) and printed on transparencies (CAD/Art Services) with a resolution of 8 μm. Silicon wafers are cleaned using piranha etching (H_2SO_4 and H_2O_2 in a 3:1 ratio) at 120 °C for 15 min, dried, and spin-coated with SU-8 2050 (Microchem) to achieve a photoresist layer of height ∼120 μm. After prebaking, the photoresist is exposed to UV with the mask aligned over it using a Karl Suss MA6 Mask Aligner. The wafer is developed after a postexposure bake using propylene glycol monomethyl ether acetate and rinsed with isopropyl alcohol. The channel depths are quantified using a profilometer (KLA-Tencor P-16). Profilometry results are included in Sec. I of the Supplemental Material [75].

The microfluidic devices are made of polydimethylsiloxane (PDMS, Sylgard-184) from Dow Corning with a 10:1 ratio of base to curing agent. The silicon wafer is treated with trichlorosilane (Gelest Inc.) in a vacuum desiccator for 20 min before pouring PDMS and baked at 70 °C for at least 4 h. The devices are then cut out and entry ports are punched using 1.5 mm biopsy punches (Miltex). The PDMS devices are sealed to glass slides (Thermo Fisher Scientific) by plasma treatment (Harrick Plasma) for 1 min and baked for at least 2 h before use. After baking, the device is rendered hydrophobic by treatment with Novec 1720 electronic grade coating (3M), which is injected into the channels. After complete evaporation of the liquid, the device is heated at 130 °C for 1 h. Furthermore, oil is injected into the device and allowed to sit overnight prior to use, to completely avoid adhesion of aqueous droplets to the device walls during the experiment. Pinning and contact line formation between the drop and the wall is avoided during experiments. Visually, pinning is easy to identify, because the drop deformation is often distorted when pinned, and the region of contact with the wall appears darker. Experiments where pinning is observed are discarded.

The sealed device is then mounted on the stage of an inverted microscope (Olympus IX 83) with a calibrated stage. Two cameras are used for imaging: a Basler ace acA1300-60gm camera with a maximum frame rate of 60 fps at 1.3 MP resolution is used for trapping the droplets using LabVIEW
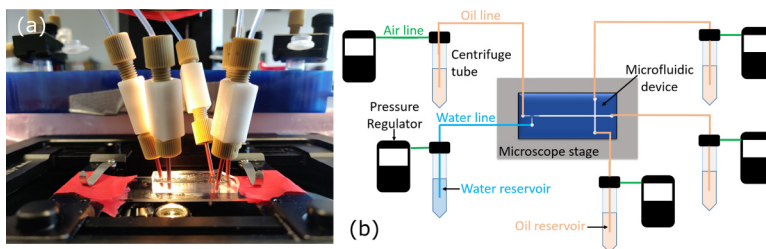
FIG. 1. (a) Experimental setup of the hydrodynamic trap for droplets, showing the microfluidic device mounted on an inverted microscope with the rigid tubing (red) used to increase flow resistance. (b) Schematic of the trapping setup, showing (1) microfluidic chip, (2) microscope stage, (3) centrifuge tubes used as reservoirs for the fluids, (4) continuous phase fluid (oil), (5) dispersed phase fluid (aqueous), (6) tubing used to deliver oil to the device, (7) tubing used to deliver aqueous phase to the device, (8) analog-controlled pressure regulators, and (9) tubing used to deliver pressurized air to the reservoirs.

(National Instruments), while a Photron Mini UX100 high speed camera is used to capture the rapid droplet deformation dynamics. The hydrodynamic trapping setup has previously been described in detail by Shenoy *et al.* [53]. Pressure regulators from Proportion Air (QPV series) are used to pressurize the headspace of air in microfluidic reservoirs (Darwin Microfluidics, XS size). The requisite pressure is converted to voltage using the following conversion: The pressure range for the regulators is 0–30 psi (gauge), and the output voltage is 0–10 V dc. The pressure in psi (gauge) is multiplied by 10/30 to convert it to voltage and this voltage signal is sent to a National Instruments Data Acquisition board with a cDAQ-9174 chassis, NI 9264 Analog Output module and NI 9201 Analog Input module, which is in turn wired to the pressure regulators. The reservoirs hold the fluids to be supplied to the microfluidic device, and are connected to the device via Teflon tubing (1.59 mm OD × 0.51 mm ID ID, IDEX Health and Science) coupled with a small section of high-flow resistance PEEKsil tubing (IDEX Health and Science, 100 μm ID) of length 5 cm with a union assembly (IDEX Health and Science) as shown in Fig. 1(a). The high-resistance tubing is sized such that the flow resistance of this section is at least 5–10 times that of the microfluidic channels due to the small inner diameter of this tubing, and it is added at each inlet of the microfluidic device. This is done to avoid back flow and trap destabilization due to small defects in microfabrication of the channels.

B. Droplet-on-demand and hydrodynamic trapping

In this work, the Stokes trap developed by Shenoy *et al.* [53] has been modified to allow for droplet generation on the same microfluidic chip. Essentially, a T-junction geometry is added upstream of the cross-slot to allow for generation of monodisperse droplets with controllable size and speed [76]. Several microfluidic geometries are available for generating monodisperse droplets, including T-junctions, coflow, and flow-focusing devices [76–78]. However, it was found that the T-junction geometry was best suited for the hydrodynamic trap, since it causes minimal disruption of the flow field in the trapping region. For hydrodynamic trapping with uniform droplet generation, the pressure of the dispersed phase is comparable to the pressure in the continuous phase, which shears off the dispersed phase at the T-junction. The Laplace pressure drop across the droplet interface for a T-junction of width 40 μm and height 90 μm is on the order of 0.1 psi (gauge) for all the oil-aqueous systems studied here, meaning that maintaining the meniscus at the T-junction intersection requires the dispersed phase pressure to be approximately 0.1 psi (gauge) higher than the continuous phase. Maintaining a fluid-fluid meniscus at the T-junction intersection is critical for generating a small number of droplets (2 or 3) using a drop-on-demand technique. The T-junction does not play a role in trapping droplets and is placed far upstream of the cross-slot geometry to avoid interference of the droplet formation process with the trapping mechanism.
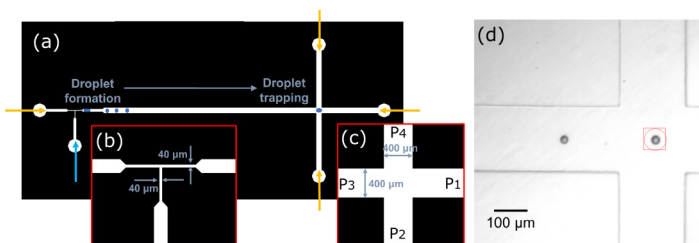
FIG. 2. (a) Microfluidic device design for the modified hydrodynamic trap, showing the location of the T-junction for droplet formation on the microfluidic chip and the four-channel cross-slot for droplet trapping on the same chip. (b) Dimensions of the T-junction for droplet formation (c) Dimensions of the cross-slot for droplet trapping, including the designations P_1–P_4 for the four channels forming the cross-slot. (d) Image of a droplet trapped in the modified hydrodynamic trap. The red square is an overlay used to indicate the desired position or "set point" for trapping, and the red circle is used to indicate the current or actual position of the droplet.

Aqueous phase droplets are generated on-demand to ensure that three or fewer droplets are generated, which can then be trapped downstream of the T-junction in the trap region. This controlled drop generation is important because the incoming droplets can often coalesce with or displace a trapped droplet in the cross-slot. If the goal of the microfluidic experiment is to trap a single droplet to study its relaxation dynamics, it is preferable to avoid interference from incoming droplets. The drop-on-demand technique is implemented using an excess pulse pressure applied to the fluid in the dispersed phase reservoir. A LabVIEW program is used to maintain a constant pressure of the dispersed phase to maintain the fluid meniscus at the intersection of the T-junction, and to apply a pulse of high pressure for a short duration to generate droplets when necessary using manual control with a Boolean switch. The actual pulse durations and pressures are tuned depending on the oil-aqueous solutions being studied.

Flow through the cross-slot microfluidic device is visualized using a 10% v/v emulsion of water in light mineral oil. Open-source PIV software (PIVlab) is used to extract flow-field information [79]. The flow field in the cross-slot contains a stagnation point near the center of the cross-slot, as seen in Fig. S2 [75]. Particles and droplets are trapped at the stagnation point in a Stokes trap using the Model Predictive Control (MPC) strategy implemented previously by Shenoy et al. [53]. Briefly, droplets that enter the region of interest, defined here as the cross-slot region, are detected using binary image processing and particle tracking in LabVIEW. To steer a droplet from its initial position to the final desired position—here the center of the cross-slot—an optimum trajectory is determined, such that the flow rates are reasonably incremented in small steps, and the particle reaches the set target position via the shortest possible trajectory. To achieve this, an optimization problem is solved by discretizing a finite time period, referred to by Shenoy et al. [53] as a finite time horizon, into intervals with a frequency equal to the sampling frequency. In this case, the sampling frequency of the image is the camera frame rate, which is set to 30 fps for the Basler ace acA1300-60gm camera (max. frame rate is 60 fps). This MPC algorithm solves for the flow rates required to steer the droplet along the shortest trajectory and is iterated after every time interval. It is implemented using the Automatic Control and Dynamic Optimization (ACADO) toolkit for solving nonlinear MPC problems [80].

Consider that the microfluidic cross-slot has i channels, where $i = 4$ for the four-channel cross-slot. The flow rates q_i in each channel of the cross-slot are calculated using the MPC algorithm. These flow rates are converted to pressures p_i using the relation $p_i = p_0 + r_i q_i$, where p_0 is a base pressure [set to 3 psi (gauge) in most cases], r_i denotes the hydrodynamic resistance in the channel, which is calculated using the formula $r_i = \frac{12\mu_o L_i}{1 - 0.63(\frac{h}{w_i})} \frac{1}{h^3 w_i}$ [50], where μ_o is the continuous phase viscosity and L_i, h, and w_i are the lengths, height, and widths of the channels, respectively. The Stokes trap for particles implemented by Shenoy et al. is a symmetric device with all the channels
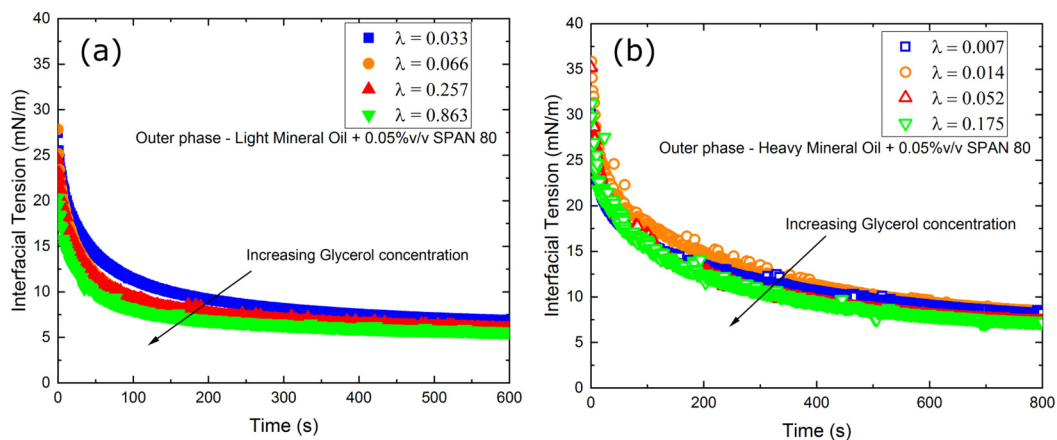
FIG. 3. (a) Interfacial tension measurements using pendant drop tensiometry for light mineral oil with 0.05% v/v SPAN 80 in the continuous phase with 0–70% aqueous glycerol in the dispersed phase. (b) Interfacial tension measurements using pendant drop tensiometry for heavy mineral oil with 0.05% v/v SPAN 80 in the continuous phase with 0–70% aqueous glycerol in the dispersed phase.

and tubing being of equal length. In the case of our modified Stokes, trap, the resistance of the microfluidic channel containing the droplet formation region is almost five times as high as that of the other three channels forming the cross-slot. Moreover, the shear rate required in the T-junction to form droplets is high, requiring high pressures to be applied to the channels of the T-junction. This gives rise to high velocity of droplets in the trap region with a net flow of droplets into the channel P_1 [Fig. 2(c)]. Therefore, rapid response of the trapping algorithm is required to capture droplets. Shenoy *et al.* [53,81] define the optimization problem for the flow rates in terms of two controller weights, denoted as β, which relates to flow rates in the channels and θ, which is a "compensation" for deviation from the set position. In general, lower values of β (10^{-5} to 10^{-4}) and higher values of θ (>1000) are found to be appropriate for trapping droplets in this experiment. These controller weights can be tuned for fluids of different viscosities.

C. Materials

In this work, we use two different continuous phases (light and heavy mineral oils, Sigma Aldrich) to vary the continuous phase viscosity. Aqueous glycerol solutions at 0%, 20%, 50%, and 70% by volume prepared using HPLC grade water (Fisher Scientific) and glycerol (Fisher Scientific) are used as the dispersed (droplet) phase for droplet deformation experiments. A nonionic surfactant, SPAN 80 (Sorbitane monooleate, Croda Inc.) at a fixed concentration of 0.05% v/v is added to the continuous phase, i.e., oil, to achieve uniform droplet formation. The equilibrium interfacial tensions of the oil-aqueous systems are measured using pendant drop tensiometry with a Drop Shape Analyzer (Krüss GmbH) at room temperature using standard protocol [82]. Note that the equilibrium interfacial tensions of all the systems studied here lie in the range of 5–10 mN/m as indicated in Fig. 3. These systems are chosen to have minimal changes in interfacial tension but large changes in viscosities. The viscosities of the aqueous glycerol solutions and the mineral oils are measured using an AR-G2 rotational rheometer (TA instruments) with a concentric cylinder geometry over a shear rate range of 1–1000 s^{-1}, and the fluids are found to be Newtonian over this shear rate range. The experiments are performed with light and heavy mineral oils in the continuous phase with dynamic viscosities (μ_o) of 26.8 mPa s and 132.2 mPa s, respectively. The dispersed phases used include water and glycerol-water solutions with viscosities (μ_i) in the range 1.73–23.13 mPa s. The viscosity ratios ($\lambda = \frac{\mu_i}{\mu_o}$) range from 0.007 to 0.863, spanning almost two orders of magnitude.
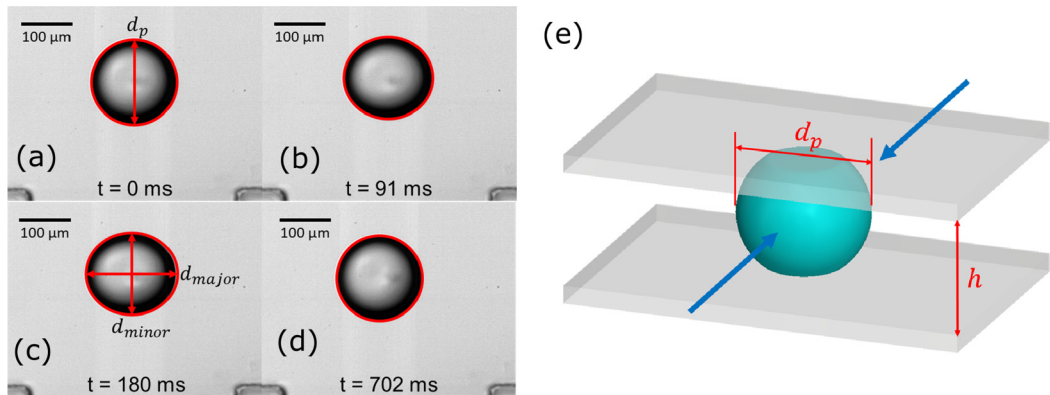
FIG. 4. (a)–(d) Droplet shape perturbation after application followed by cessation, of a pressure pulse at various instants of time, showing deformation and relaxation of droplet shape. The original undeformed projected droplet diameter d_p and the lengths of the major and minor axes of the deformed droplet (d_{major} and d_{minor}) are indicated in panels (a) and (c), respectively. (e) Sketch of the droplet confined by the walls of the microfluidic device, showing the direction of the applied pressure pulse (blue arrows) and the channel height h compared with the projected drop diameter d_p.

III. RESULTS AND DISCUSSION

A. Droplet deformation in a microfluidic hydrodynamic trap

Droplets trapped at the center of the cross-slot in the microfluidic trap are deformed by applying an excess pressure pulse of 10 psi to channels P_2 and P_4 [see Figs. 2(a)–2(c)]. A pulse pressure of 10 psi is chosen to induce measurable deformation of a trapped droplet while also keeping it trapped at the center of the cross-slot. Projected droplet diameters (d_p, measured in top view) are in the range 90–250 μm, with the device height h being $\sim$90 μm on average (due to PDMS channel swelling by mineral oils). Device height after swelling is measured using the calibrated Z-stage of the inverted microscope. Prior to the application of excess pressure, the droplet is in its equilibrium configuration and has a squished spherical or pancake-like shape. After application of the pressure pulse, the droplet assumes an ellipsoidal shape as shown in Figs. 4(b) and 4(c). The pulse is applied for a period of 50 ms, after which the excess pressure is reduced to zero, while the droplet is still trapped. This allows the droplet to relax back to its equilibrium configuration. The droplet is imaged in two dimensions (i.e., in top view) for approximately 1 s, such that it appears circular prior to deformation and elliptical after the pressure pulse is applied. High speed videos of droplet shape relaxation are captured at a frame rate of 12 500 fps using the Photron Mini UX 100 camera. These videos are then analyzed in MATLAB using a custom image analysis code [6,14] which detects projected droplet diameter and major and minor axes lengths. The deformed shape of the droplet is described by a deformation parameter D, coined by Taylor in his pioneering studies on droplet deformation in emulsions [17,18]. Here

$$D = \frac{d_{major} - d_{minor}}{d_{major} + d_{minor}}, \tag{1}$$

where d_{major} and d_{minor} are the lengths of the major and minor axes of the ellipse respectively.

The image analysis yields the droplet deformation parameter D as a function of time, and the timestamp is obtained from the frame rate. The variation of D as a function of time for the system consisting of light mineral oil in the continuous phase with 50% glycerol-water solution in the dispersed phase, for droplets of various projected diameters is shown in Fig. 5(a). Initially, D sees a sharp increase as the droplet is deformed, and the droplet gradually relaxes back to its equilibrium shape when the pressure pulse is stopped. The maximum deformation D_{max} attained by a droplet of
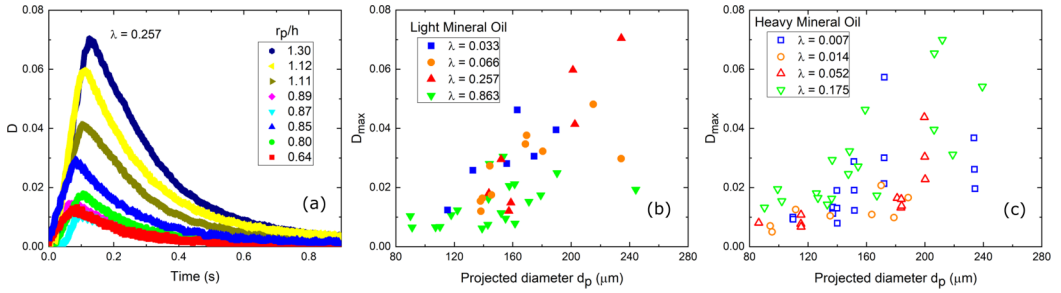
FIG. 5. (a) Droplet deformation D as a function of time for the system containing 50% glycerol-water solution in the dispersed phase with light mineral oil in the continuous phase ($\lambda = 0.257$). Different symbols indicate droplets with different initial projected radii ($r_p = d_p/2$), and the channel height (h) is taken to be 90 μm. Droplets attain highly deformed shapes, followed by relaxation back to equilibrium. (b) Maximum deformation as a function of projected diameter for aqueous glycerol systems (0%, 20%, 50%, 70%) in light mineral oil. (c) Maximum deformation as a function of projected diameter for aqueous glycerol systems (0%, 20%, 50%, 70%) in heavy mineral oil.

a given size under the applied pressure pulse increases with an increase in d_p. This trend in $D_{\max}$ as a function of projected diameter is shown in Figs. 5(b) and 5(c). $D_{\max}$ does not appear to show any dependence on the viscosity ratio. Linear scaling for $D_{\max}$ as a function of d_p is shown in Figs. S4(a) and S4(b), while Fig. S4(c) shows that the slopes of the lines do not exhibit a meaningful dependence on viscosity ratio [75]. $D_{\max}$ has previously been used by researchers to study droplet deformation due to forcing by an extensional flow field in microfluidic contraction-expansion geometries, to measure interfacial tension [43,83]. Here the focus is on the droplets' intrinsic relaxation time (τ), driven by droplet size and material properties of the two fluids after sudden cessation of flow, rather than $D_{\max}$.

An exponential decay is fit to the drop shape relaxation curves, such as those depicted in Fig. 5(a), starting at the maximum observed deformation, and is given by

$$D = D_0 + D_{\max}\, e^{-\frac{t}{\tau}}, \tag{2}$$

where D_0 is the equilibrium deformation, $D_{\max}$ is the deformation at time $t = 0$, and τ is the relaxation time obtained from fitting Eq. (2) to the drop shape decay curves. When a droplet is deformed by the pressure pulse, the viscous stress in the continuous phase acts to deform the droplet, while interfacial tension between the two liquid phases acts to restore droplet shape. Similarly, as the droplet shape relaxes back to equilibrium, the interfacial tension and viscous stress in the continuous phase act as competing forces. A detailed discussion on the competing forces influencing droplet deformation is provided in the following sections. When the continuous phase is much more viscous than the dispersed phase, the dispersed phase viscosity is not considered as a major parameter influencing the droplet's shape relaxation. Here we test this hypothesis by changing the dispersed phase viscosity relative to the continuous phase, while keeping the interfacial tension approximately constant. If the forcing flow is approximately the same for all cases, one may then seek to study the dependence of the relaxation time on the fluid properties and the droplet's confinement in the channel. In other words, $\tau = f(r_p,\ h,\ \mu_i, \mu_o, \gamma)$, where $r_p = \frac{d_p}{2}$ is the projected radius. A simple dimensional analysis reveals the existence of three dimensionless parameters as follows:

$$\frac{\tau \gamma}{h \mu_w} = f\left(\frac{r_p}{h}, \frac{\mu_i}{\mu_o}\right). \tag{3}$$
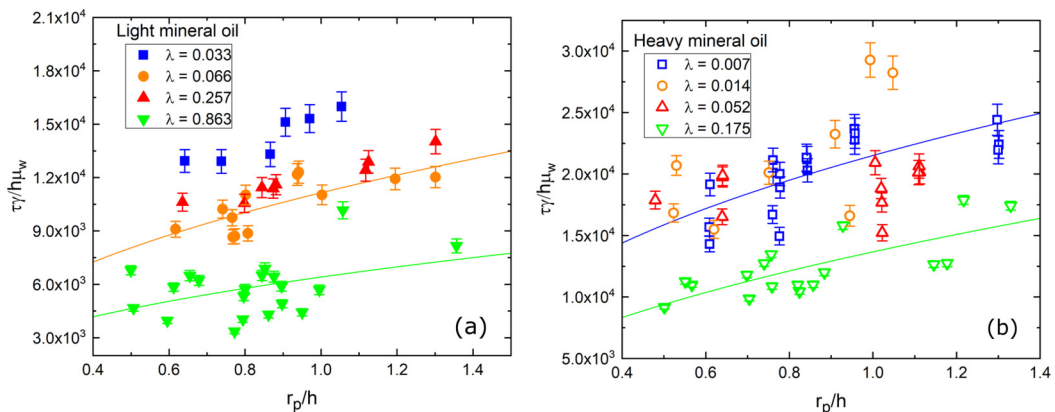
FIG. 6. (a), (b) Dimensionless droplet shape relaxation time as a function of confinement ratio for (a) light mineral oil and (b) heavy mineral oil in the continuous phase with 0%, 20%, 50%, and 70% aqueous glycerol in the dispersed phase. The error bars indicate propagated uncertainty arising from uncertainty in the relaxation time fits and interfacial tension and channel height measurements. The solid lines are examples of power-law fits to the relaxation time data with corresponding colors.

In the above equation, the first dimensionless parameter is a modified capillary number, where a reference viscosity $\mu_w = 1$ mPa s has been used, while the second is the confinement ratio $\frac{r_p}{h}$ and the third is the viscosity ratio $\frac{\mu_i}{\mu_o}$. The variation of the relaxation time with the confinement ratio $\frac{r_p}{h}$ is shown in Figs. 6(a) and 6(b) with 0%, 20%, 50%, and 70% glycerol-water solutions in the dispersed phase and light and heavy mineral oils in the continuous phase, respectively. Across the entire range of viscosity ratios, it is found that the relaxation time increases with an increase in $\frac{r_p}{h}$. A power-law curve can be fit to the data using the relation $\frac{\tau\gamma}{h\mu_w} = a(\frac{r_p}{h})^b$ at any given viscosity ratio. Examples of these power-law fits are shown in both Figs. 6(a) and 6(b). The goodness-of-fit parameters (R^2), and the fitting parameters a and b for each system are provided in the Supplemental Material [75]. With light mineral oil in the continuous phase and across the entire range of viscosity ratios, the exponent b of the power-law fit ranges from 0.42 to 0.49, indicating approximately a $\frac{\tau\gamma}{h\mu_w} \sim \sqrt{\frac{r_p}{h}}$ scaling. Similar exponents in the 0.44–0.61 range are found for heavy mineral oil in the continuous phase, although larger scatter in the data resulted in poor fitting for the 50% glycerol-water case. The average value of the exponent is 0.47 ± 0.06.

The droplet deformation experiments in this work involve neither unconfined ($\frac{r_p}{h} \ll 1$) nor highly confined ($\frac{r_p}{h} \gg 1$) droplets. In fact, Balsa [84] and Thompson [85] probed the validity of the Hele-Shaw assumption for confined flow around a cylindrical object, and found that the assumption breaks down at large separations, leading to secondary flows with streamwise vorticity arising from the boundary layer around the object. To satisfy the Hele-Shaw assumption, it is generally accepted that the confinement ratio $\frac{r_p}{h}$ must exceed 4 [66,68], which is not the case in any of the experiments in this work. To the best of our knowledge, no theory exists for describing droplet deformation and relaxation in the weak to moderate confinement regime, leaving tremendous potential for studying the rich flow features in this problem. According to the empirical scaling relation developed in Eq. (3), we find that the relaxation time varies with projected radius approximately as $\tau \sim \sqrt{\frac{r_p}{h}}$, with the exact scaling factor being 0.47. Figure 7 shows the normalized deformation $\frac{D}{D_{\max}}$ plotted as a function of the rescaled time $t_1 = t(\frac{h}{r_p})^{0.47}$ for 50% glycerol-water droplets in light mineral oil, according to the empirical scaling developed in Fig. 6. All the deformation curves collapse after rescaling, indicating that the decay time is indeed proportional to approximately the square root of the radius in the weak to moderate confinement regime. Similar plots showing collapse of the
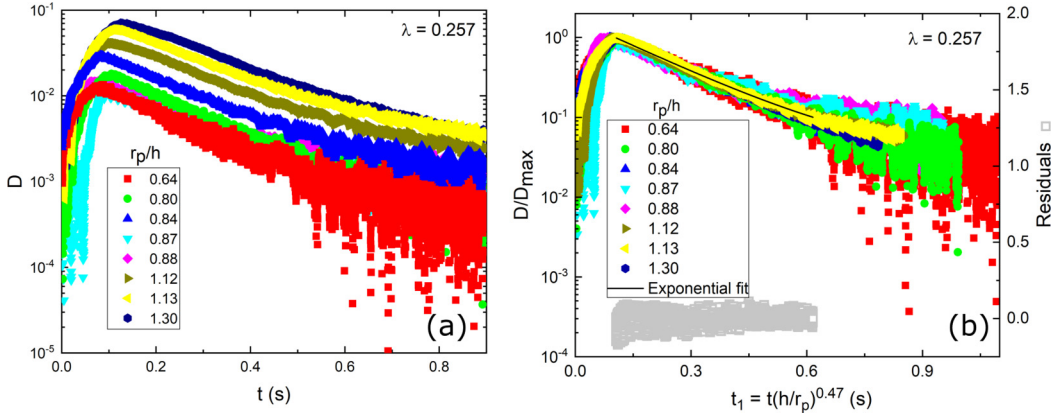
FIG. 7. (a) Droplet deformation versus time for the light mineral oil–50% aqueous glycerol system ($\lambda = 0.257$) at various droplet sizes. The channel height h is taken to be 90 μm. (b) Normalized deformation $\frac{D}{D_{max}}$ (left axis) as a function of rescaled time $t_1 = t(\frac{h}{r_p})^{0.47}$, for the same system. The black line is an exponential decay fit to the collapsed droplet shape relaxation curve. The residuals for the fit are indicated on the right axis, with a goodness-of-fit parameter $R^2 = 0.98$.

droplet deformation curves and exponential fits to the collapsed data for other viscosity ratios in this study are included in the Supplemental Material [75]. Note that this scaling is applicable for the confinement ratio ($\frac{r_p}{h}$) range of ~0.5–1.4, and should not in any way be considered a master curve for all confinement ratios. Further, the relaxation time obtained from a single collapsed curve is compared to that obtained from individually fitting exponential decays to the scaled curves for individual droplet sizes in the Supplemental Material, to indicate the collapse obtained from the scaling. Fig. 7(b) shows one such exponential curve obtained by fitting a single exponential decay to the collapsed data. The relaxation time (τ') obtained from this fit is related to the original relaxation times at various droplet radii (r_p) via $\tau' = \tau(\frac{h}{r_p})^{0.47}$. This scaled relaxation time encapsulates the droplet size dependence, but varies with viscosity ratio.

The role of the dispersed phase in drop shape relaxation is discussed in literature dating back to work by Lamb [16] and Chandrasekhar [19], which examines shape oscillation and damping of a viscous liquid sphere in a fluid of negligible viscosity. These derivations show that oscillations are suppressed for a viscosity exceeding a "critical viscosity" defined by Chandrasekhar [19], and droplet shape relaxes exponentially to equilibrium. For a drop suspended in a fluid of negligible viscosity (e.g., in air), the relaxation time varies inversely as the droplet's viscosity. With light mineral oil in the continuous phase, it is observed that the relaxation time exhibits a weak dependence on the dispersed phase viscosity (or the viscosity ratio λ) in the low viscosity ratio limit as shown in Fig. 6(a). For the 70% aqueous glycerol solution in light mineral oil, the viscosity ratio increases substantially compared to all the other cases ($\lambda = 0.863$), and the viscosity of the droplet phase nearly equals that of the continuous phase. In this case, we observe that the droplet shape relaxation time is notably lower. This decrease in relaxation time indicates that for a highly viscous droplet, the energy dissipation inside the droplet (in the boundary layer on the droplet side) becomes significant, leading to rapid return to the equilibrium shape. Lee *et al.* [86] found that for a highly confined stationary droplet with fluid flowing around it, the circulation inside the droplet phase is strongest close to the liquid-liquid interface. This finding may suggest that the droplet relaxation time can be influenced by the dispersed phase viscosity and the change in circulation inside the droplet as the pressure pulse is removed. Similarly, as shown in Fig. 6(b), with heavy mineral oil in the continuous phase, the relaxation time is smaller for the highest viscosity ratio of 0.175, although the difference is not as evident as is the case with light mineral oil in the continuous phase. The scaled relaxation
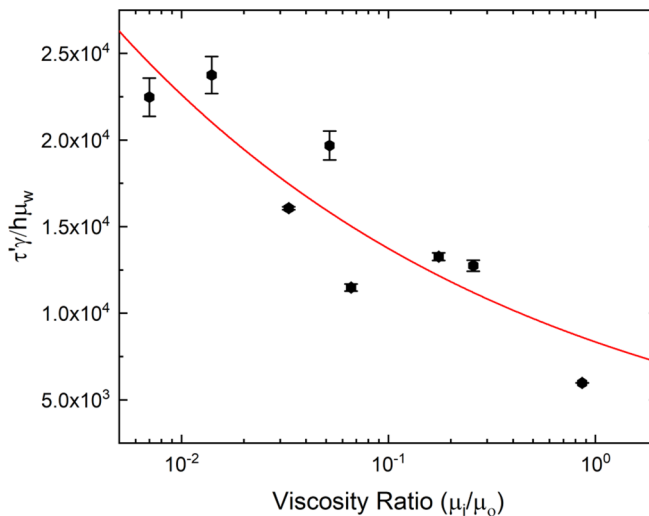
FIG. 8. Dimensionless scaled relaxation time $\tau' = \tau(\frac{h}{r_p})^{0.47}$, as a function of viscosity ratio. The solid line indicates a power-law fit to the data, with a goodness-of-fit parameter $R^2 = 0.8$. The error bars on the data points indicate propagated uncertainty arising from uncertainty in the relaxation time fits and interfacial tension and channel height measurements.

time $\tau' = \tau(\frac{h}{r_p})^{0.47}$ obtained from fitting an exponential decay to the collapsed data in Fig. 7(b) and Figs. S6 and S7 can now be plotted against the viscosity ratio ($\frac{\mu_i}{\mu_o}$), as shown in Fig. 8 in dimensionless form. The scaled relaxation time can be related to the viscosity ratio using another power-law fit as $\frac{\tau'\gamma}{h\mu_w} = x(\frac{\mu_i}{\mu_o})^y$, as shown in Fig. 8 by the solid line. The exponent y is approximately equal to -0.22 ± 0.12. Combining the confinement and viscosity ratio dependence, an empirical equation for the relaxation time can be written as

$$\tau = K\frac{h}{\gamma}\left(\frac{r_p}{h}\right)^{0.47\pm0.06}\left(\frac{\mu_i}{\mu_o}\right)^{-0.22\pm0.12}, \tag{4}$$

where K is a constant equal to $\sim 8.34 \pm 3.74$ in these experiments.

B. Theory for droplet shape relaxation in unconfined and confined flows

The characteristic timescale for a free droplet's relaxation to equilibrium was derived by Taylor and others [18,30,43,83] for an initially spherical droplet in an unconfined flow field in the limit of very small to moderate viscosity ratios. This timescale, called the viscous dissipation time, is a function of the droplet radius ($r = \frac{a_0}{2}$), viscosity ratio (λ), interfacial tension (γ), and either the continuous (μ_o) or dispersed (μ_i) phase viscosity. Additionally, a_0 is the diameter of a spherical droplet having the same volume as a pancake-shaped confined droplet with a projected diameter d_p, and is calculated using the formula $a_0 = \sqrt[3]{h^3 + \frac{3h}{2}(d_p - h)(\frac{\pi h}{2} + d_p - h)}$ [87,88], where h is the height of the microfluidic channel. d_p is obtained from the experiments, and the calculated diameter a_0 is the diameter of an unconfined spherical droplet having the same volume as the confined pancake-shaped droplet when $d_p > h$, and is taken to be equal to d_p when $d_p < h$. Here we define the viscous dissipation timescale in terms of the continuous phase viscosity to illustrate order-of-magnitude trends compared with the experimentally measured relaxation time. However, it is important to be aware of the viscosity ratio range ($\lambda \ll 1$) in which this theoretical viscous
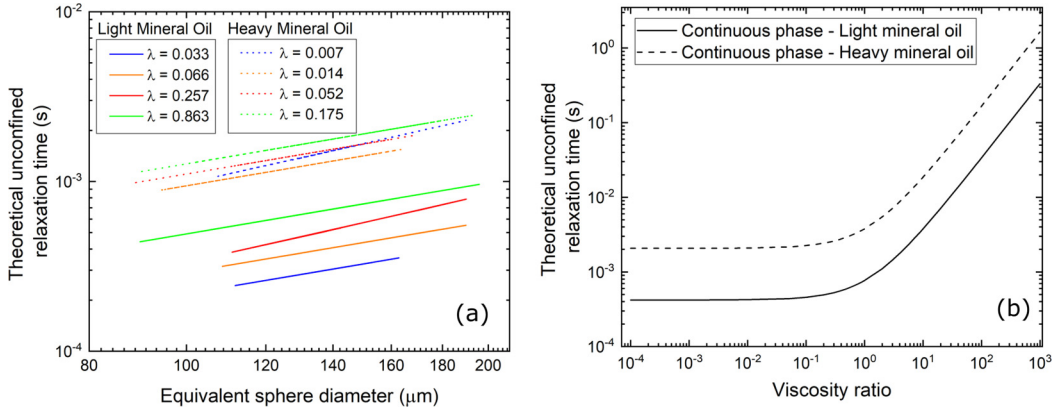
FIG. 9. (a) Theoretical relaxation time for unconfined droplets as a function of droplet diameter over the range of droplet diameters and viscosity ratios in this study. (b) Theoretical relaxation time for unconfined droplets as a function of viscosity ratio for a droplet of equivalent sphere diameter 157 μm with an interfacial tension of 6 mN/m.

dissipation time ($\tau_{\text{visc}-c}$) is valid [30]. It is given by

$$\tau_{\text{visc}-c} = \frac{\alpha \mu_o r}{\gamma}, \tag{5}$$

where the parameter α is a function of the viscosity ratio λ, and is given by

$$\alpha = \frac{(2\lambda + 3)(19\lambda + 16)}{40(\lambda + 1)}. \tag{6}$$

Figure 9(a) shows the characteristic relaxation time for droplets over a range of drop sizes (same volume as the range investigated in this work) calculated using Eq. (5). It can be seen that in the unconfined case, i.e. for a droplet relaxing to equilibrium in a quiescent, infinite fluid reservoir, the droplet relaxation time is driven by two key parameters, namely the continuous phase viscosity and the interfacial tension. Since the viscosity of light mineral oil is lower, the relaxation time is smaller than the heavy mineral oil cases, similar to the trend observed in our experiments with confined droplets. Moreover, it is interesting to note that the viscosity ratio does not strongly affect the relaxation time when the viscosity ratio is small ($\lambda \ll 1$) as seen in Fig. 9(b), whereas the curve begins to deviate and increase substantially as the viscosity ratio approaches 1.

In comparison, there does not exist any theory for weakly or moderately confined droplet relaxation time, where the relaxation of droplet shape is affected by the presence of the walls of the microfluidic device, even though there exists a film of oil between the droplet and the top and bottom walls of the device. The other limiting case which has been studied numerically is the highly confined regime, where the droplet is sandwiched between plates in a Hele-Shaw geometry. A numerical scheme for the shape evolution of highly confined pancake-shaped droplets in microfluidic channels was developed by Gallaire and coworkers [66–68], when $\frac{r_p}{h} \gg 1$. A model for analyzing flow through porous media, Darcy's law, is modified to include a correction for the depth-averaged Laplacian, yielding the Brinkman equations [66–68], which are then solved numerically [66–68] using the boundary element method. Brun *et al.* [66] investigated the relaxation of a stationary droplet inside a microfluidic channel using this scheme, and found that a rescaling of the time t as $t' = t \frac{h^2}{r_p^2}$ leads to collapse of the droplet shape relaxation curves. In other words, in the highly confined limiting regime, it was found via numerical solutions that the relaxation time varies

as the square of the projected droplet radius, while theory for the completely unconfined regime shows that the relaxation time varies as the radius of the spherical droplet.

C. Comparison of experimental and theoretical relaxation times

Finally, a comparison of Fig. 6 and Fig. 9 sheds light on another important difference between the experimentally measured droplet shape relaxation times and the theoretical relaxation time for free, unconfined droplets. The relaxation time for unconfined droplets ($\tau_{\mathrm{visc}-c}$) of the same volumes and with the same continuous and dispersed phase viscosities and interfacial tensions is approximately two orders of magnitude smaller than the experimentally measured relaxation times for confined droplets. This observation is qualitatively in agreement with previous work investigating droplet shape relaxation in confined flows. For example, Vananroye et $al.$ [61] studied the relaxation of polydimethylsiloxane droplets in polyisobutylene upon cessation of shear flow and found that highly confined droplets relax much slower than unconfined or moderately confined droplets. Moreover, for extensional flow around a confined, moving droplet, Brosseau [83] found that the experimental relaxation time lags behind the theoretical relaxation time by an order of magnitude. Tiwari et $al.$ [89] also found that the relaxation time of droplets following pinch-off of a liquid bridge in a Hele-Shaw cell increases with increase in confinement. Janssen and Anderson [90] argue that the slower relaxation of confined droplets is because the fluid in the continuous phase must be squeezed out of the thin film between the droplet and the wall during droplet relaxation, leading to an additional resistance, making it a problem of thin film drainage.

For confined droplets, the drag force exerted by the confining walls is thought to influence the droplet relaxation, and in general, causes the relaxation to lag that for an unconfined droplet. Two-dimensional micro-PIV by Ulloa et $al.$ [65] has shown that in a cross-slot flow, the vorticity remains negligible everywhere except at the corners of the cross-slot. Therefore, while the confinement of the droplet by the top and bottom walls of the device affects drop dynamics, the side walls and corners of the cross-slot are far enough from the droplet that they are not expected to influence the droplet relaxation. As mentioned earlier, it is well-known that for microconfined droplets that do not wet the device walls, a thin lubrication layer exists between the droplet and the wall, and its thickness has been estimated to be within 0.1–3 μm for pancake-shaped droplets in microchannels [91–94]. However, it is possible and even likely that the thickness of the lubrication layer between the droplet and the wall evolves during the droplet shape relaxation as the fluid in the film drains out. Since the droplet has a weak confinement in the microfluidic device, it is reasonable to expect the thickness of the lubrication layer to vary slightly from the edge of the droplet to the center. As the pulse pressure is applied to deform the droplet, there will be an influx of the continuous phase into the thin film between the droplet and the wall, thereby changing locally the curvature of the film in proximity to the wall. Moreover, as the pulse pressure is released, the excess fluid in the film will drain out, and the curvature will relax back to its original state. Janssen and Anderson [90] showed that the thin film may even dimple as the droplet relaxes. The capillary force driving droplet relaxation would be balanced by the viscous dissipation in the thin film. This is potentially why we see higher relaxation times with the more viscous heavy mineral oil in the continuous phase as shown in Figs. 6(a) and 6(b). Moreover, due to the weak to moderate confinement of droplets in the experiments presented here, the problem is a fully three-dimensional one, possibly with complex secondary flows [84,85], and none of the limiting cases are applicable. A full hydrodynamic analysis of the lubrication force on weakly or moderately confined droplets will be a subject of future work. A hydrodynamic analysis for moving droplets in a capillary, and with varying viscosity ratios, was carried out by Lac and Sherwood [95], whereas analysis of bubbles in microconfined flows was done by Rabaud et $al.$ [96]. Models for film thickness around highly confined droplets in capillaries or microfluidic devices over a range of capillary numbers can be found in work by Balestra et $al.$ [97].
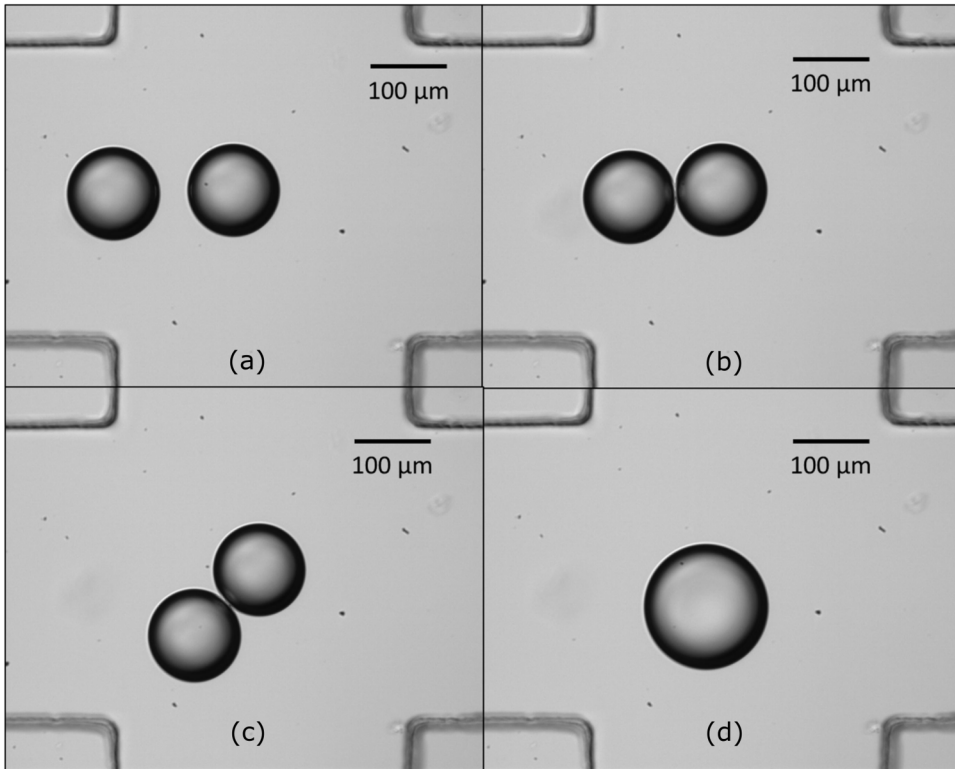
FIG. 10. Coalescence of an incoming droplet with a droplet trapped at the center of the cross-slot showing the various stages of coalescence. The system shown here consists of confined water droplets in light mineral with 0.01% v/v SPAN 80, studied in detail in Narayan *et al.* [59].

D. Outlook for droplet shape relaxation during coalescence

Droplet shape relaxation studies find application in several interesting problems in multiphase flows. One such problem is droplet coalescence in micro-confined environments. Here a single droplet is trapped at the center of the hydrodynamic trap, and a series of incoming droplets are allowed to coalesce with the trapped droplet, as demonstrated in a recent work by the authors' group [59]. Figures 10(a)–10(d) show the coalescence of water droplets in light mineral oil with 0.01% v/v SPAN 80 in the continuous phase. Immediately following coalescence, the coalesced droplet attains a highly distorted geometry, which ultimately relaxes back to a circular pancake shape as shown in Fig. 10(d). These highly distorted dumbbell-like initial shapes and their relaxation back to a circular shape can be strongly influenced by the fluid properties, surfactant gradients after coalescence, as well as the confinement of the droplet in the microfluidic device. Further, using the hydrodynamic trap, it is possible to measure the film drainage time for droplet coalescence. Droplet coalescence in linear flows occurs in three stages, namely, (1) approach of the droplets from a starting separation distance, (2) contact between droplets and drainage of the thin film between them, during which droplets may rotate about a common axis, and (3) rupture of the thin film, leading to coalescence and formation of highly distorted droplet shapes which eventually relax to a circular shape [98]. It is well documented in the literature that the film drainage time for droplet coalescence is a function of the droplet velocity, surfactant concentration, droplet size and fluid properties [98–100]. Future work using the hydrodynamic trap will allow a detailed investigation of these parameters on drop shape relaxation during coalescence, as showed by our initial study of surfactant and hydrodynamic effects on droplet coalescence using this geometry in Narayan *et al.* [59].

IV. CONCLUSIONS

In this work, a "Stokes trap" previously developed by Shenoy *et al.* [53] is modified for two-phase liquid-liquid systems to include on-chip droplet formation using a drop-on-demand technique. This work is the first such application of the microfluidic hydrodynamic trap to measure transient droplet response to perturbations, to the best of our knowledge. The droplet shape relaxation time is measured from the drop shape decay curves. It is found that the droplet shape relaxation time depends on the confinement ratio $\frac{r_p}{h}$ and the viscosity ratio λ. It is found that larger continuous phase viscosity results in longer relaxation times. This is because the lubrication layer of the continuous phase between the droplet and the wall must drain to allow restoration of droplet shape. A comparison of experimentally measured relaxation times for confined droplets with theoretical relaxation times for unconfined droplets reveals that the experimentally measured relaxation times for confined droplets of the same volume are orders of magnitude larger than the unconfined case. Additionally, it is also found that the relaxation times for weakly to moderately confined droplets, such as the ones in this study, do not exhibit the same radius scaling as either the limiting unconfined ($\frac{r_p}{h} \ll 1$) or highly confined ($\frac{r_p}{h} \gg 1$) cases. Instead, a $\tau \sim \sqrt{\frac{r_p}{h}}$ scaling for the relaxation time is found from the experiments in this study.

The results of this work have implications for the behavior of confined droplets in various emulsion processing applications including during transients such as flow start-up and sudden cessation, leading to relaxation of droplet shape. The results obtained indicate that while the viscosity ratios have a small impact on drop shape relaxation, the effect of confinement is much more dominant compared to unconfined droplets. Previous work has also shown that the presence of surfactants can lead to Marangoni effects along the droplet interface during deformation and may impart a dilatational elasticity to the interface [101–103]. Lee *et al.* [86] observed that this Marangoni flow can impact the circulation inside the droplet in the highly confined limit. A rigid, surfactant-laden droplet interface may also exhibit different relaxation behavior. It is unclear whether these gradients can strongly influence the drop dynamics in this study. Future work will investigate any potential impact of surfactant gradients on droplet deformation and coalescence.

[1] T. Zhang, D. Davidson, S. L. Bryant, and C. Huh, *Nanoparticle-Stabilized Emulsions for Applications in Enhanced Oil Recovery*, in SPE Improved Oil Recovery Symposium (Society of Petroleum Engineers, Tulsa, Oklahoma, USA, 2010).

[2] S. Cobos, M. S. Carvalho, and V. Alvarado, Flow of oil-water emulsions through a constricted capillary, Int. J. Multiphase Flow **35**, 507 (2009).

[3] C. Charcosset, Preparation of emulsions and particles by membrane emulsification for the food processing industry, J. Food Eng. **92**, 241 (2009).

[4] P. Fischer and E. J. Windhab, Rheology of food materials, Curr. Opin. Colloid Interface Sci. **16**, 36 (2011).

[5] S. Friberg, K. Larsson, and J. Sjoblom, *Food Emulsions* (CRC Press, 2003).

[6] A. R. Metcalf, H. C. Boyer, and C. S. Dutcher, Interfacial tensions of aged organic aerosol particle mimics using a biphasic microfluidic platform, Environ. Sci. Technol. **50**, 1251 (2016).

[7] S. S. Davis, C. Washington, P. West, L. Illum, G. Liversidge, L. Sternson, and R. Kirsh, Lipid emulsions as drug delivery systems, Ann. NY Acad. Sci. **507**, 75 (1987).

[8] C. W. Pouton, Formulation of self-emulsifying drug delivery systems, Adv. Drug. Deliv. Rev. **25**, 47 (1997).

[9] C.-X. Zhao, Multiphase flow microfluidics for the production of single or multiple emulsions for drug delivery, Adv. Drug. Deliv. Rev. **65**, 1420 (2013).

[10] C. Gallegos and J. M. Franco, Rheology of food, cosmetics and pharmaceuticals, Curr. Opin. Colloid Interface Sci. **4**, 288 (1999).

[11] D. Miller, E.-M. Wiener, A. Turowski, C. Thunig, and H. Hoffmann, O/W emulsions for cosmetics products stabilized by alkyl phosphates—Rheology and storage tests, Colloids Surf. A **152**, 155 (1999).

[12] D. J. Miller, T. Henning, and W. Grünbein, Phase inversion of W/O emulsions by adding hydrophilic surfactant—A technique for making cosmetics products, Colloids Surf. A **183-185**, 681 (2001).

[13] E. J. Windhab, M. Dressler, K. Feigl, P. Fischer, and D. Megias-Alguacil, Emulsion processing—From single-drop deformation to design of complex processes and products, Chem. Eng. Sci. **60**, 2101 (2005).

[14] S. Narayan, D. B. Moravec, B. G. Hauser, A. J. Dallas, and C. S. Dutcher, Removing water from diesel fuel: Understanding the impact of droplet size on dynamic interfacial tension of water-in-fuel emulsions, Energy Fuels **32**, 7326 (2018).

[15] Lord Rayleigh, On the instability of jets, Proc. Lond. Math. Soc. **s1–10**, 4 (1878).

[16] H. Lamb, Hydrodynamics, *Hydrodynamics* (Cambridge University Press, Cambridge, 1932).

[17] G. I. Taylor, The viscosity of a fluid containing small drops of another fluid, Proc. R. Soc. Lond. A **138**, 41 (1932).

[18] G. I. Taylor, The formation of emulsions in definable fields of flow, Proc. R. Soc. Lond. A **146**, 501 (1934).

[19] S. Chandrasekhar, *Hydrodynamic and Hydromagnetic Stability* (Courier Corporation, 2013).

[20] Y. Bayazitoglu and P. V. R. Suryanarayana, Dynamics of oscillating viscous droplets immersed in viscous media, Acta Mech. **95**, 167 (1992).

[21] C. A. Miller and L. E. Scriven, The oscillations of a fluid droplet immersed in another fluid, J. Fluid Mech. **32**, 417 (1968).

[22] Y. Tian, R. G. Holt, and R. E. Apfel, A new method for measuring liquid surface tension with acoustic levitation, Rev. Sci. Instrum. **66**, 3349 (1995).

[23] H.-L. Lu and R. E. Apfel, Quadrupole oscillations of drops for studying interfacial properties, J. Colloid Interface Sci. **134**, 245 (1990).

[24] C.-J. Hsu and R. E. Apfel, A technique for measuring interfacial tension by quadrupole oscillation of drops, J. Colloid Interface Sci. **107**, 467 (1985).

[25] A. Prosperetti, Free oscillations of drops and bubbles: The initial-value problem, J. Fluid Mech. **100**, 333 (1980).

[26] D. Barthes-Biesel and A. Acrivos, Deformation and burst of a liquid droplet freely suspended in a linear shear field, J. Fluid Mech. **61**, 1 (1973).

[27] R. G. Cox, The deformation of a drop in a general time-dependent fluid flow, J. Fluid Mech. **37**, 601 (1969).

[28] J. M. Rallison, A numerical study of the deformation and burst of a viscous drop in general shear flows, J. Fluid Mech. **109**, 465 (1981).

[29] J. M. Rallison and A. Acrivos, A numerical study of the deformation and burst of a viscous drop in an extensional flow, J. Fluid Mech. **89**, 191 (1978).

[30] J. M. Rallison, The deformation of small viscous drops and bubbles in shear flows, Annu. Rev. Fluid Mech. **16**, 45 (1984).

[31] E. J. Hinch and A. Acrivos, Long slender drops in a simple shear flow, J. Fluid Mech. **98**, 305 (1980).

[32] B. R. Bzdek, R. M. Power, S. H. Simpson, J. P. Reid, and C. Patrick Royall, Precise, contactless measurements of the surface tension of picolitre aerosol droplets, Chem. Sci. **7**, 274 (2016).

[33] R. M. Power and J. P. Reid, Probing the micro-rheological properties of aerosol particles using optical tweezers, Rep. Prog. Phys. **77**, 074601 (2014).

[34] R. M. Power, S. H. Simpson, J. P. Reid, and A. J. Hudson, The transition from liquid to solid-like behaviour in ultrahigh viscosity aerosol particles, Chem. Sci. **4**, 2597 (2013).

[35] B. J. Bentley and L. G. Leal, An experimental investigation of drop deformation and breakup in steady, two-dimensional linear flows, J. Fluid Mech. **167**, 241 (1986).

[36] D. C. Tretheway and L. G. Leal, Deformation and relaxation of Newtonian drops in planar extensional flows of a Boger fluid, J. Non-Newtonian Fluid Mech. **99**, 81 (2001).

[37] H. A. Stone and L. G. Leal, Relaxation and breakup of an initially extended drop in an otherwise quiescent fluid, J. Fluid Mech. **198**, 399 (1989).

[38] H. A. Stone, B. J. Bentley, and L. G. Leal, An experimental study of transient effects in the breakup of viscous drops, J. Fluid Mech. **173**, 131 (1986).

[39] J.-W. Ha and L. G. Leal, An experimental study of drop deformation and breakup in extensional flow at high capillary number, Phys. Fluids **13**, 1568 (2001).

[40] G. F. Christopher, J. Bergstein, N. B. End, M. Poon, C. Nguyen, and S. L. Anna, Coalescence and splitting of confined droplets at microfluidic junctions, Lab Chip **9**, 1102 (2009).

[41] T. Cubaud, Deformation and breakup of high-viscosity droplets with symmetric microfluidic cross flows, Phys. Rev. E **80**, 026307 (2009).

[42] S. D. Hudson, J. T. Cabral, W. J. Goodrum Jr, K. L. Beers, and E. J. Amis, Microfluidic interfacial tensiometry, Appl. Phys. Lett. **87**, 081905 (2005).

[43] Q. Brosseau, J. Vrignon, and J.-C. Baret, Microfluidic dynamic interfacial tensiometry (μDIT), Soft Matter **10**, 3066 (2014).

[44] J. T. Cabral and S. D. Hudson, Microfluidic approach for rapid multicomponent interfacial tensiometry, Lab Chip **6**, 427 (2006).

[45] Q. Zhou, Y. Sun, S. Yi, K. Wang, and G. Luo, Investigation of droplet coalescence in nanoparticle suspensions by a microfluidic collision experiment, Soft Matter **12**, 1674 (2016).

[46] Y.-J. Lin, A. Perrard, S. L. Biswal, R. M. Hill, and S. Trabelsi, Microfluidic investigation of asphaltenes-stabilized water-in-oil emulsions, Energy Fuels **32**, 4903 (2018).

[47] Y.-C. Tan, Y. L. Ho, and A. P. Lee, Droplet coalescence by geometrically mediated flow in microfluidic channels, Microfluid. Nanofluid. **3**, 495 (2007).

[48] J. Wei Khor, N. Jean, E. S. Luxenberg, S. Ermon, and S. K. Y. Tang, Using machine learning to discover shape descriptors for predicting emulsion stability in a microfluidic channel, Soft Matter **15**, 1361 (2019).

[49] S. D. Hudson, F. R. Phelan, M. D. Handler, J. T. Cabral, K. B. Migler, and E. J. Amis, Microfluidic analog of the four-roll mill, Appl. Phys. Lett. **85**, 335 (2004).

[50] M. Tanyeri, M. Ranka, N. Sittipolkul, and C. M. Schroeder, A microfluidic-based hydrodynamic trap: design and implementation, Lab Chip **11**, 1786 (2011).

[51] M. Tanyeri and C. M. Schroeder, Manipulation and confinement of single particles using fluid flow, Nano Lett. **13**, 2357 (2013).

[52] M. Tanyeri, E. M. Johnson-Chavarria, and C. M. Schroeder, Hydrodynamic trap for single particles and cells, Appl. Phys. Lett. **96**, 224101 (2010).

[53] A. Shenoy, C. V. Rao, and C. M. Schroeder, Stokes trap for multiplexed particle manipulation and assembly using fluidics, Proc. Natl. Acad. Sci. USA **113**, 3976 (2016).

[54] D. Kumar, A microfluidic device for producing controlled collisions between two soft particles, Thesis, University of Toronto, 2016.

[55] Y. Zhou and C. M. Schroeder, Single polymer dynamics under large amplitude oscillatory extension, Phys. Rev. Fluids **1**, 053301 (2016).

[56] C. M. Schroeder, Single polymer dynamics for molecular rheology, J. Rheol. **62**, 371 (2018).

[57] S. Goel, N. Joshi, M. S. Uddin, S. Ng, E. Acosta, and A. Ramachandran, Interfacial tension of the water-diluted bitumen interface at high bitumen concentrations measured using a microfluidic technique, Langmuir **35**, 15710 (2019).

[58] A. H. Motagamwala, A microfluidic, extensional flow device for manipulating soft particles, Thesis, University of Toronto, 2013.

[59] S. Narayan, I. Makhnenko, D. B. Moravec, B. G. Hauser, A. J. Dallas, and C. S. Dutcher, Insights into the microscale coalescence behavior of surfactant-stabilized droplets using a microfluidic hydrodynamic trap, Langmuir **36**, 9827 (2020).

[60] M. K. Mulligan and J. P. Rothstein, The effect of confinement-induced shear on drop deformation and breakup in microfluidic extensional flows, Phys. Fluids **23**, 022004 (2011).

[61] A. Vananroye, P. Van Puyvelde, and P. Moldenaers, Effect of confinement on the steady-state behavior of single droplets during shear flow, J. Rheol. **51**, 139 (2007).

[62] M. Minale, Models for the deformation of a single ellipsoidal drop: A review, Rheol. Acta **49**, 789 (2010).

[63] M. Minale, A phenomenological model for wall effects on the deformation of an ellipsoidal drop in viscous flow, Rheol. Acta **47**, 667 (2008).

[64] M. Minale, S. Caserta, and S. Guido, Microconfined shear deformation of a droplet in an equiviscous non-Newtonian immiscible fluid: Experiments and modeling, Langmuir **26**, 126 (2010).

[65] C. Ulloa, A. Ahumada, and M. L. Cordero, Effect of confinement on the deformation of microfluidic drops, Phys. Rev. E **89**, 033004 (2014).

[66] P.-T. Brun, M. Nagel, and F. Gallaire, Generic path for droplet relaxation in microfluidic channels, Phys. Rev. E **88**, 043009 (2013).

[67] M. Nagel and F. Gallaire, Boundary elements method for microfluidic two-phase flows in shallow channels, Comput. Fluids **107**, 272 (2015).

[68] M. Nagel, P.-T. Brun, and F. Gallaire, A numerical study of droplet trapping in microfluidic devices, Phys. Fluids **26**, 032002 (2014).

[69] M. Kerdraon, J. D. McGraw, B. Dollet, and M.-C. Jullien, Self-Similar Relaxation of Confined Microfluidic Droplets, Phys. Rev. Lett. **123**, 024501 (2019).

[70] K. Verhulst, R. Cardinaels, P. Moldenaers, S. Afkhami, and Y. Renardy, Influence of viscoelasticity on drop deformation and orientation in shear flow. Part 2: Dynamics, J. Non-Newtonian Fluid Mech. **156**, 44 (2009).

[71] A. Luciani, M. F. Champagne, and L. A. Utracki, Interfacial tension coefficient from the retraction of ellipsoidal drops, J. Polym. Sci. B **35**, 1393 (1997).

[72] Y. Xia and G. M. Whitesides, Soft lithography, Annu. Rev. Mater. Sci. **28**, 153 (1998).

[73] J. C. McDonald and G. M. Whitesides, Poly (dimethylsiloxane) as a material for fabricating microfluidic devices, Acc. Chem. Res. **35**, 491 (2002).

[74] D. Qin, Y. Xia, and G. M. Whitesides, Soft lithography for micro-and nanoscale patterning, Nat. Protoc. **5**, 491 (2010).

[75] See Supplemental Material at http://link.aps.org/supplemental/10.1103/PhysRevFluids.5.113603 for profilometry and viscosity measurements, PIV data, D_{max} analysis, and data collapse with radius scaling.

[76] G. F. Christopher and S. L. Anna, Microfluidic methods for generating continuous droplet streams, J. Phys. D Appl. Phys. **40**, R319 (2007).

[77] S. L. Anna, Droplets and bubbles in microfluidic devices, Annu. Rev. Fluid Mech. **48**, 285 (2016).

[78] A. R. Metcalf, S. Narayan, and C. S. Dutcher, A review of microfluidic concepts and applications for atmospheric aerosol science, Aerosol Sci. Technol. **52**, 310 (2018).

[79] W. Thielicke and E. Stamhuis, PIVlab—Towards user-friendly, affordable and accurate digital particle image velocimetry in matlab, J. Open Res. Softw. **2**, e30 (2014).

[80] B. Houska, H. J. Ferreau, and M. Diehl, ACADO toolkit—An open-source framework for automatic control and dynamic optimization, Optimal Control Appl. Methods **32**, 298 (2011).

[81] A. Shenoy, D. Kumar, S. Hilgenfeldt, and C. M. Schroeder, Flow Topology During Multiplexed Particle Manipulation Using a Stokes Trap, Phys. Rev. Appl. **12**, 054010 (2019).

[82] J. D. Berry, M. J. Neeson, R. R. Dagastine, D. Y. Chan, and R. F. Tabor, Measurement of surface and interfacial tension using pendant drop tensiometry, J. Colloid Interface Sci. **454**, 226 (2015).

[83] Q. Brosseau, Dynamics of soft interfaces in droplet-based microfluidics, Thesis, Georg-August-Universität Göttingen, 2014.

[84] T. F. Balsa, Secondary flow in a Hele-Shaw cell, J. Fluid Mech. **372**, 25 (1998).

[85] B. W. Thompson, Secondary flow in a Hele-Shaw cell, J. Fluid Mech. **31**, 379 (1968).

[86] S. Lee, F. Gallaire, and C. N. Baroud, Interface-induced recirculation within a stationary microfluidic drop, Soft Matter **8**, 10750 (2012).

[87] L. Nandy and C. S. Dutcher, Phase behavior of ammonium sulfate with organic acid solutions in aqueous aerosol mimics using microfluidic traps, J. Phys. Chem. B **122**, 3480 (2018).

[88] S. M. Vuong, A microfluidic platform for the control and analysis of phase transitions in concentrating droplets, Thesis, Carnegie Mellon University, 2014.

[89] D. Tiwari, L. Mercury, M. Dijkstra, H. Chaudhary, and J. F. Hernández-Sánchez, Post-pinch-off relaxation of two-dimensional droplets in a Hele-Shaw cell, Phys. Rev. Fluids **3**, 124202 (2018).

[90] P. J. A. Janssen and P. D. Anderson, Boundary-integral method for drop deformation between parallel plates, Phys. Fluids **19**, 043602 (2007).

[91] F. P. Bretherton, The motion of long bubbles in tubes, J. Fluid Mech. **10**, 166 (1961).

[92] L. Zhu and F. Gallaire, A pancake droplet translating in a Hele-Shaw cell: Lubrication film and flow field, J. Fluid Mech. **798**, 955 (2016).

[93] A. Huerre, O. Theodoly, A. M. Leshansky, M.-P. Valignat, I. Cantat, and M.-C. Jullien, Droplets in Microchannels: Dynamical Properties of the Lubrication Film, Phys. Rev. Lett. **115**, 064501 (2015).

[94] H. Chen, Q. Meng, and J. Li, Thin lubrication film around moving bubbles measured in square microchannels, Appl. Phys. Lett. **107**, 141608 (2015).

[95] E. Lac and J. D. Sherwood, Motion of a drop along the centreline of a capillary in a pressure-driven flow, J. Fluid Mech. **640**, 27 (2009).

[96] D. Rabaud, P. Thibault, J.-P. Raven, O. Hugon, E. Lacot, and P. Marmottant, Manipulation of confined bubbles in a thin microchannel: Drag and acoustic Bjerknes forces, Phys. Fluids **23**, 042003 (2011).

[97] G. Balestra, L. Zhu, and F. Gallaire, Viscous Taylor droplets in axisymmetric and planar tubes: From Bretherton's theory to empirical models, Microfluid. Nanofluid. **22**, 67 (2018).

[98] L. G. Leal, Flow induced coalescence of drops in a viscous fluid, Phys. Fluids **16**, 1833 (2004).

[99] Y. T. Hu, D. J. Pine, and L. G. Leal, Drop deformation, breakup, and coalescence with compatibilizer, Phys. Fluids **12**, 484 (2000).

[100] H. Yang, C. C. Park, Y. T. Hu, and L. G. Leal, The coalescence of two equal-sized drops in a two-dimensional linear flow, Phys. Fluids **13**, 1087 (2001).

[101] H. Brenner, *Interfacial Transport Processes and Rheology* (Elsevier, 2013).

[102] D. Langevin, Influence of interfacial rheology on foam and emulsion properties, Adv. Colloid Interface Sci. **88**, 209 (2000).

[103] D. Langevin, Rheology of adsorbed surfactant monolayers at fluid surfaces, Annu. Rev. Fluid Mech. **46**, 47 (2014).